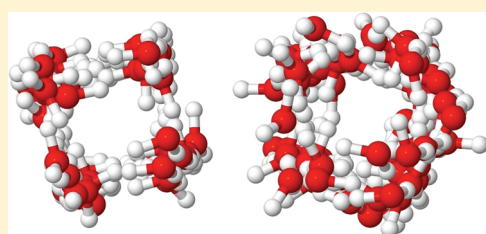


# Simulation Study of Structural, Transport, and Thermodynamic Properties of TIP4P/2005 Water in Single-Walled Carbon Nanotubes

Christa Guse and Reinhard Hentschke\*

Fachbereich Mathematik und Naturwissenschaften, Bergische Universität, D-42097 Wuppertal, Germany

**ABSTRACT:** Because carbon nanotubes lack a strong interaction with water, its hydrogen bond network is altered mainly by the confining geometry alone, allowing one to study its influence on the structure of water. Here structural, transport, and thermodynamic properties are investigated for TIP4P/2005 water confined in single-walled carbon nanotubes, possessing diameters from 11 to 50 Å. Temperatures range from 220 to 600 K for the two pressures studied, 1 and 1000 atm. The results, based on grand canonical Monte Carlo techniques, include heats of adsorption, temperature and diameter dependent densities, density profiles, diffusion constants, and pressure tensor components. The main findings comprise the suppression of the density maximum in tubes with diameters below 50–25 Å, indicating that structures responsible for this anomaly are of comparable size. Furthermore the axial pressure can be described within the continuum limit with deviations only appearing for diameters below 20 Å. The diffusion constants are similar to that of bulk water, demonstrating that the agility of the hydrogen bond network is preserved in the confining geometries considered here.



## INTRODUCTION

As carbon nanotubes (CNTs) lack a strong interaction with water, its hydrogen bond network is altered mainly by the confining geometry alone. Therefore, CNTs provide an ideal medium for the study of the hydrogen-bond network of water under extreme conditions.

A number of experimental and simulation studies have been performed in order to connect the behavior of bulk water in the supercooled region to that of confined water cooled below the homogeneous nucleation line, in order to gain insight into the phase diagram of bulk water in its experimentally inaccessible region and to close the gap between the amorphous and liquid forms of water. The main experimental observations include evidence for a fragile-to-strong dynamic crossover transition in confined water in the range between 190 and 280 K<sup>1</sup> and for the breakdown of the Stokes–Einstein relation.<sup>2</sup> Simulation results of bulk water<sup>3</sup> attributed this behavior to a crossover between a high density and a low density liquid. These results aroused our interest in the question of how much of water's anomalous structural behavior persists in confinement.

Previous studies by Koga et al.<sup>4</sup> and Byl et al.<sup>5</sup> concentrated on the phase behavior of confined water, finding a number of order-to-disorder phase transitions between ice ring structures and liquid water. Martí and Gordillo computed the vibrational and rotational spectra of confined water<sup>6</sup> and investigated the gradual destruction of the hydrogen-bond network together with faster diffusive regimes with increasing temperature inside carbon nanotubes.<sup>7</sup> Another question of theoretical and technical importance was discussed by Striolo et al.,<sup>8–10</sup> who investigated the condensation transition of water in carbon nanotubes and sheets with and without chemical heterogeneities. They found in agreement with Birkett and Do<sup>11</sup> that the presence and distribution of oxygenated sites such as carbonyl, hydroxyl, or carboxyl groups

exert a strong effect on the adsorption isotherms and the width of the observed hysteresis. It was also shown in several studies that the wettability of narrow carbon nanotubes is strongly influenced by the carbon–water interaction potentials.<sup>12–14</sup>

In ref 15, the authors describe molecular dynamics (MD) simulations of CNTs completely submerged in liquid SPC/E (simple point charge/extended) and TIP3P (transferable intermolecular potential 3 point) water reservoirs at constant atmospheric pressure. In this fashion, in difference to most other studies, the water molecules can adsorb on the outside of the CNTs and also interact with water molecules inside. Pascal et al. study the various contributions to the free energy difference between bulk water and confined water to clarify the driving forces behind the filling of the CNTs with water. Their computation of molecular translational, vibrational, and rotational entropy effects on adsorption adds complementary information to the present study. In particular, they obtain a favorable free energy under confinement due to increased rotational and translational entropy for narrow CNTs and mainly due to increased translational entropy for wider CNTs.

This investigation of TIP4P/2005 water in confinement, which follows a simulation study of bulk water by our group,<sup>16</sup> is intended to throw further light on differences and similarities in the structure and thermodynamic properties of confined and unconfined water. We use grand canonical Monte Carlo (GCMC) simulations to determine radial density profiles and axial pair correlation functions as well as thermodynamic properties such as energy and pressure of water in single-walled carbon nanotubes (SWNTs). We find that the confinement of water

**Received:** October 24, 2011

**Revised:** December 13, 2011

**Published:** December 15, 2011

frustrates the hydrogen bond network strongly, leading to a varied phase behavior with the occurrence of several different ice phases in small tubes. While the behavior becomes more bulklike in intermediate tubes, the constrictions suppress the development of a density maximum even in tubes with a diameter of 26 Å. It is only in the widest 49.5 Å tubes that we find a density maximum though at a lower temperature than in the bulk liquid. This indicates that “cluster” structures thought to be responsible for the density anomaly should be of comparable size. For the axial pressure, we observe deviations from the continuum limit for tube diameters below 20 Å, while extrapolations show that CNTs containing bulk water must at least be 500 Å in diameter.

Another motivation to study the vicinal phases of water in CNTs stems from its unusually enhanced transport properties, observed both experimentally<sup>17</sup> and in simulation,<sup>18</sup> which make CNTs similar to biological water channels and open up possible applications as novel drug delivery agents or water filters. Thus, in addition, we perform MD simulations and determine the diffusion constant parallel and perpendicular to the tube axis, confirming an enhancement in diffusion compared to bulk water. We try to characterize the properties of confined water systematically in dependence on tube diameter, temperature, and pressure.

## METHODS

**Water Model for Confined Water.** As was pointed out by Alexiadis and Kassinos,<sup>18</sup> the water models proposed for bulk water are generally not correct for confined water. But they show by investigating six different flexible and nonflexible water models in rigid and flexible tubes that the general trend of density, hydrogen bond number, and diffusion does not depend on the specific water or tube model. We thus limit our investigation to rigid carbon nanotubes filled by TIP4P/2005 water, as we found this water model to perform best in the bulk simulations.<sup>16</sup>

**Chemical Potential.** In order to perform a Monte Carlo simulation in the grand canonical ensemble, we need to determine the chemical potential of liquid TIP4P/2005<sup>19</sup> water at all thermodynamic conditions of interest. Attempts to compute the chemical potential by Widom’s test particle insertion method<sup>20,21</sup> from configurations generated by previous MD computations of liquid water in the NPT ensemble failed due to poor convergence. Therefore, we applied the overlapping distribution method of Shing and Gubbins,<sup>22</sup> as it improves on the Widom insertion method by combining insertion and deletion of molecules to gain more information about the system.

In order to test if our results for the chemical potential are self-consistent, we use thermodynamic integration. Provided the chemical potential is known at one state point it is possible to obtain additional values by integration in the  $T, P$  plane, i.e.

$$\frac{\mu(T, P)}{T} = \frac{\mu(T_0, P)}{T_0} - \int_{T_0}^T \frac{h}{T^2} dT \quad (1)$$

along isobars

$$\mu(T, P) = \mu(T, P_0) + \int_{P_0}^P \frac{dP}{\rho} \quad (2)$$

along isotherms. Here  $h$  is the enthalpy per molecule and  $\rho$  is the density, which were taken from our own MD simulations of the TIP4P/2005 water and from Pi et al.<sup>23</sup>

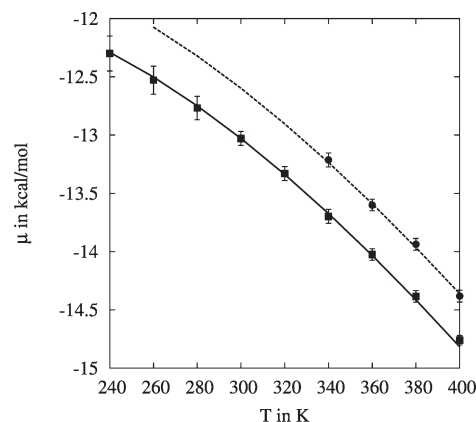


**Figure 1.** Chemical potential of TIP4P/2005 water vs temperature. Symbols: Shing–Gubbins at 1 bar (squares) and 1000 bar (circles). Lines: thermodynamic integration at 1 bar (solid line) and 1000 bar (dashed line).

First we compute the chemical potential on the coexistence line<sup>24</sup> at  $T = 550$  K and  $\rho = 0.0213$  g/cm<sup>3</sup> and  $P = 38$  bar by Widom’s insertion method. This is possible because of the low density. Thus, we arrive at  $\mu = -18.38$  kcal/mol, which is close to the ideal gas value of  $\mu = -18.73$  kcal/mol as expected. Because the chemical potential is the same on both sides of the coexistence line, we can now compute  $\mu$  at a different state point in the liquid phase by eqs 1 and 2.

Figure 1 shows our final result for the chemical potential as it was computed by the Shing–Gubbins method and by thermodynamic integration for several pressures and temperatures. The agreement is excellent, giving us confidence that we now have reliable values for the chemical potential of TIP4P/2005 water at temperatures higher than 240 K which we can use for our grand canonical ensemble simulations. We also want to perform simulations in the low temperature range ( $<240$  K), where the chemical potential cannot be determined precisely enough by the Shing–Gubbins method. We therefore use the values obtained by thermodynamic integration in this temperature region.

As a final consistency check, we perform a Monte Carlo simulation at  $T = 320$  K with  $\mu = -13.33$  kcal/mol and test if the density converges to the molecular dynamics value of  $\rho = 0.9896$  g/cm<sup>3</sup>. As a start configuration for the GCMC run, we take a MD configuration generated at  $T = 280$  K and a density of  $\rho = 1.0001$  g/cm<sup>3</sup>. The convergence is slow because the probabilities of insertion and deletion are small in the dense fluid. The average equilibrium density of the GCMC simulation is 0.9899 g/cm<sup>3</sup> which is very close to the expected density.

**Carbon Nanotubes and Carbon–Water Interaction.** The smallest SWNTs successfully synthesized have a diameter of 4 Å,<sup>25</sup> while the most frequent diameter encountered for most high yield synthesis techniques is  $\approx 14$  Å. Diameters wider than 25 Å are only rarely reported. In our simulations, we observe a filling of the nanotubes with water at atmospheric pressures only for diameters larger than  $\approx 11$  Å which seems to be a direct consequence of our choice of carbon–water interaction parameters, which will be discussed further down. We therefore limit our investigation to tube diameters from 11 to 26 Å. We only use armchair structures with diameters ((8,8) 11.00 Å; (9,9) 12.38 Å; (10,10) 13.75 Å; (11,11) 15.13 Å; (12,12) 16.50 Å; (13,13) 17.88 Å; (14,14) 19.25 Å; (16,16) 22.00 Å; (18,18) 24.75 Å).

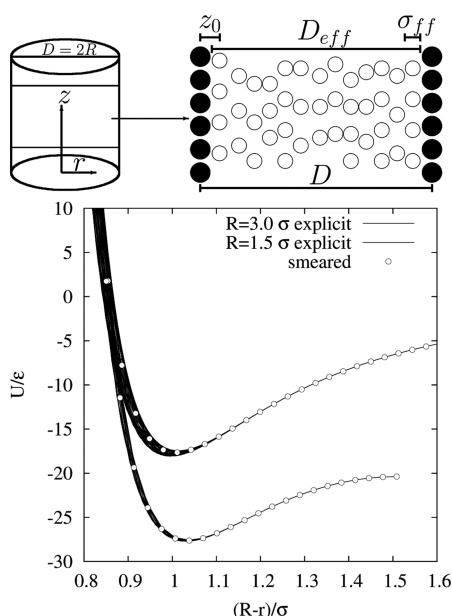


**Figure 2.** Top: Computation of the effective diameter  $D_{\text{eff}} = D - (2z_0 - \sigma_{\text{ff}})$ . Bottom: Potential  $U$  of carbon nanotubes of radius  $1.5\sigma_{\text{CO}}$  and  $3.0\sigma_{\text{CO}}$  against the distance  $(R - r)$  to the tube wall. The smeared potential (points) is shown in comparison to the explicit potential (lines) calculated using the actual carbon atom positions in an armchair configuration. The spread in the explicit potential lines is due to the different local carbon environment near the surface, which is more pronounced for a larger tube diameter (upper curve).

In order to make contact with bulk water, we also study a (36,36) 49.50 Å diameter tube.

We use periodic boundary conditions in the direction of the tube's long axis. This dimension is chosen as long as possible to avoid frustration effects on solid structures forming at certain thermodynamic conditions. The diameter-to-length ratio is at least 1/3 exclusive of the (36,36) tube whose length is 60 Å.

Instead of considering the interaction of the water molecules with each carbon atom explicitly, we use a smeared potential, which can be computed by integrating over the rolled up carbon sheet of surface density  $\theta$ . Thus, the explicit geometry of the carbon nanotube does only enter our computations through the constraints on its possible diameter. For an explanation of our nomenclature, see the upper left part of Figure 2.

The potential at distance  $r = Rx$  from the axis of a single-walled nanotube is given by Stan and Cole<sup>26</sup>

$$U(r; R) = 3\pi\theta\epsilon\sigma^2 \left[ \frac{21}{32} \left( \frac{\sigma}{R} \right)^{10} M_{11}(x) - \left( \frac{\sigma}{R} \right)^4 M_5(x) \right] \quad (3)$$

where  $\theta$  is the surface density of C atoms,  $R$  is the radius of the tube, and

$$M_n(x) = \int_0^\pi d\phi \frac{1}{(1 + x^2 - 2x \cos \phi)^{n/2}} \quad (4)$$

where  $n$  is a positive integer.

We compute the exact potential of a water molecule in a long 60 Å tube far away from the edges to see the spread in the potential due to the local carbon environment. The results are shown in Figure 2, bottom. The spread increases with the

diameter of the tube and is largest for a carbon sheet, but remains generally small. Our assumption that a smeared potential suffices to describe the behavior of water in CNTs is further strengthened by a study of Wang et al.<sup>27</sup> which found only a negligible helicity effect for the tube diameters investigated in this work.

We limit our investigation to single-walled carbon nanotubes as it was shown by Rana and Chandra<sup>28</sup> that the thickness of the nanotube wall has only minor effects on the density profiles, the hydrogen bond network, and the wetting characteristics.

There exists a broad range of water–carbon interaction potentials in the literature. As far as we can establish, all of them are based on a pairwise additive Lennard–Jones (LJ) potential between the oxygen atoms of the water and the carbon atoms  $U(r) = 4\epsilon_{\text{CO}}((\sigma_{\text{CO}}/r)^{12} - (\sigma_{\text{CO}}/r)^6)$ . Some models also include a carbon–hydrogen LJ interaction and an electrostatic interaction between the partially charged sites on the water molecules and point quadrupole moments on the carbons. An overview is given in Werder et al.<sup>29</sup> As it is difficult to judge which parametrization is superior to others, we put the emphasis on simplicity and comparability and use the potential of Bojan and Steele<sup>30</sup> because it is very common and consists just of a LJ potential between the oxygen and the carbon. They use experimental low-coverage isotherm data of  $\text{O}_2$  on exfoliated graphite to obtain the first two virial coefficients for this adsorbate over a range of temperatures. The results are then compared with the virial expression of the LJ potential yielding  $\epsilon_{\text{CO}} = 0.3135$  kJ/mol and  $\sigma_{\text{CO}} = 3.19$  Å. It is important to note that the condensation transition and thus the filling of the tubes is sensitive to the choice of the water–carbon interaction parameter as pointed out by Hummer et al.<sup>12</sup> In order to characterize the adsorption–desorption behavior of water for the chosen carbon–water interaction, we investigate the filling of carbon nanoslits.

## RESULTS AND DISCUSSION

**Adsorption Behavior of Water.** The general view on the process of water absorption in porous carbons<sup>31</sup> distinguishes three different stages. It is believed that the first water molecules are adsorbed on oxygen containing functional groups on the carbon surface, e.g., carbonyl, hydroxyl, and carboxyl groups. This view is supported by the proportionality between the number density of such active sites and water adsorption.<sup>32</sup> Experimental adsorption isotherms of water vapor on oxygenated carbon<sup>33</sup> show that by heating the substrate to different temperatures and thus reducing the amount of active sites the adsorption decreases by nearly a factor of 10. A similar effect was observed on porous carbon,<sup>34</sup> where the reduction in primary centers leads to a shift of adsorption and desorption to higher pressures and to a slight broadening of the hysteresis.

It is therefore not implausible that on a substrate without oxygenated sites, as assumed in our simulations, adsorption might be suppressed even stronger, leading to a noticeable uptake of water only above the saturation pressure. This point was also investigated in a simulation study by Birkett and Do.<sup>11</sup> They found that they could not reproduce experimental data for water on highly graphitized carbon black without including active sites into their simulations. Even with the strongest carbon–water interaction tested, the adsorption was less than 1% of the experimentally observed one at 302.15 K.

At intermediate loading, where the inflection point of the isotherm is situated, adsorption seems to be governed by cluster formation which is based on the cooperative behavior in water.



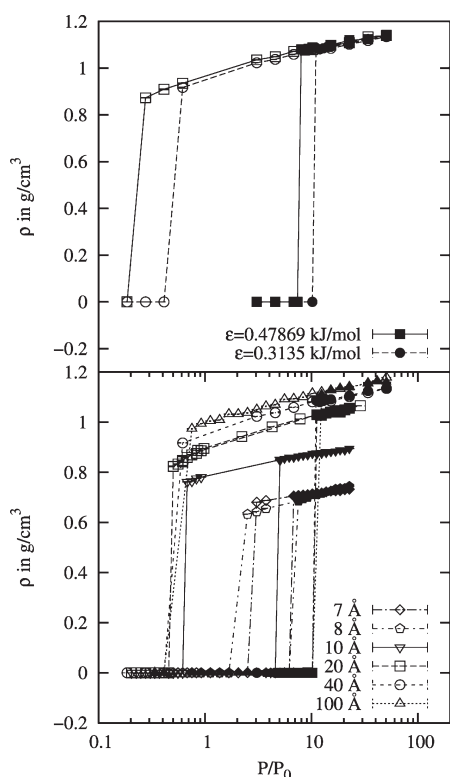


**Figure 3.** Adsorption (filled symbols) and desorption (open symbols) isotherms at 300 K against relative pressure ( $P_0$  saturation pressure). Top: for  $\epsilon = 0.47869$  kJ/mol and  $\epsilon = 0.3135$  kJ/mol at fixed geometry in a  $40 \text{ \AA}$ ,  $25.92 \times 25.92 \text{ \AA}^2$  slit. Bottom: for different geometries at  $\epsilon = 0.3135$  kJ/mol.

Our simulation data indicate that the pore size and the carbon–water potential parameters are of special importance for the exact position of the inflection and the width of the hysteresis loop. Finally, the adsorption volume becomes crowded with molecules and the adsorption isotherm levels off to a plateau region.

We simulated TIP4P/2005 water adsorption on carbon slits ranging in width from 7 to 100 Å by GCMC applying periodic boundary conditions in the directions parallel to the slit and treating the long-range Coulomb interaction by the ELC (electrostatic layer correction) method.<sup>35</sup> We carried out at least 500 million GCMC steps. We observed capillary condensation in all cases. In equilibrium, the filled slits contain about 260 molecules (for the  $7 \times 50 \times 50 \text{ \AA}^3$  slit) to 1700 molecules (for the  $100 \times 25 \times 25 \text{ \AA}^3$  slit). As described in a paper by Brennan et al.<sup>34</sup> the isosteric heat of adsorption,  $q_{st}$ , calculated from isotherms for which the first measured point is at  $P/P_0 \approx 0.1$ , here  $P_0$  is the saturation pressure, is very close to the latent heat of bulk water condensation, indicating that the formation of water clusters around primary sites must occur at very low relative pressure.

This observation of early cluster formation is in agreement with our simulation results. In the typical course of pore filling during a GCMC simulation, a small cluster builds near the carbon wall, which then grows until the whole slit is filled. While during desorption water begins to retreat from one or both walls of the slit until the whole pore is empty. We can thus note that while the creation of an initial cluster is required for adsorption, the desorption mechanism is simpler (the dynamics of capillary drying in the case of wetted, weakly adsorbing carbon slits was

discussed in detail by Leung et al.<sup>36</sup>). This is of special importance regarding the comparability of our simulations with experiment, as we do not include any active sites, which enhance cluster formation and are present experimentally in even the purest carbon samples. Our results for the desorption are thus more suitable for comparison with experiment, although the evaporation might also be influenced by the presence of primary adsorption centers.

In order to define the density of water in a carbon slit or carbon nanotube, it is necessary to determine the slit width or internal tube diameter accessible to the fluid  $D_{\text{eff}}$ , which may vary with external factors such as temperature and pressure. Here we use an expression proposed by Kaneko et al.<sup>37</sup> for carbon slit pores, which can be extended to nanotubes,<sup>38</sup> i.e.,

$$D_{\text{eff}} = D - (2z_0 - \sigma_{\text{ff}}) \quad (5)$$

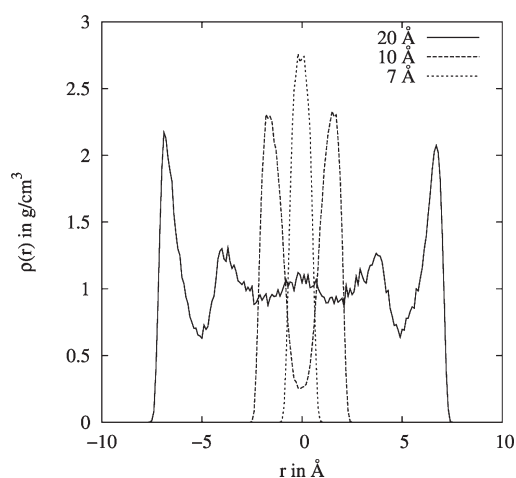
where  $\sigma_{\text{ff}}$  is a measure of the fluid particle size and  $z_0$  is the distance of closest approach between the fluid and the wall, which can be estimated by the zero-crossing of the fluid-wall potential (see the upper right part of Figure 2).  $z_0$  depends only weakly on the tube radius  $R$ . For the tube sizes considered in this work, it deviates only by 0.1% from the value for a carbon sheet. Thus, we will use the sheet value  $z_0 = 0.85837\sigma_{\text{fs}}$  to compute  $D_{\text{eff}}$ . Thus,  $D_{\text{eff}} = D - 2.3175 \text{ \AA}$ .

Figure 3 shows our simulation results for different geometries and water–carbon interactions. The upper panel presents the adsorption and desorption isotherms at 300 K for two different values of the carbon–water interaction parameter  $\epsilon$  depending on  $P/P_0$ , where  $P_0$  is the saturation pressure. We used the ideal value of the chemical potential for our simulations, having established that the chemical potential at the saturation pressure at 300 K of TIP4P/2005 water is given by its ideal value.

While capillary condensation during adsorption occurs at very high pressure in comparison to experiment for both potentials, which may be connected to the lack of active sites, evaporation happens at a more reasonable value. An increase in  $\epsilon$  from 0.3135 to 0.47869 kJ/mol, decreases the width of the hysteresis and shifts the capillary condensation and evaporation transitions to lower pressures.

Experimentally, the adsorption is determined by the pore size distribution of the substrate as well as by its purity. The condensation of water on Charcoal S84 for example occurs at  $0.8P_0$ , while evaporation happens at  $0.67P_0$ .<sup>39</sup> Also according to Gregg and Sing,<sup>39</sup> condensation happens on graphitized charcoal at about  $0.8P_0$  and evaporation at  $0.6P_0$ . Adding 4.6% of oxygenated surface groups<sup>34</sup> shifts condensation to  $0.65P_0$  and evaporation to  $0.5P_0$ , reducing the hysteresis.

For a comparison to experiment, the results of Kaneko et al. are quite interesting,<sup>40</sup> as they investigate the adsorption of water in dependence on the micropore structure, determined gravimetrically by  $\text{N}_2$  adsorption at 77 K, and the number of active sites. The comparison between PIT-5 (pore width 0.75 nm) and PIT-20 (pore width 1.13 nm) samples shows reduction of hysteresis with decreasing pore size and a shift of condensation from 0.7 to  $0.42P_0$  and of evaporation from 0.5 to  $0.4P_0$ . This is not in total agreement with our simulation results (see Figure 3 bottom), as the evaporation in small slits is shifted to considerably higher pressures, while condensation occurs at a smaller pressure for  $D = 10 \text{ \AA}$  but at increasing pressure for  $D = 8 \text{ \AA}$  and  $D = 7 \text{ \AA}$ . The dependence of pore evaporation and condensation on the slit size is weak for slits larger than 20 Å, while the hysteresis is much



**Figure 4.** Density profile of different slit geometries.

reduced for slit diameters of 7 and 10 Å in agreement with experiment.

The observed difference is in agreement with simulation studies of Striolo et al.<sup>8</sup> They find a similar pattern, where the hysteresis narrows with decreasing slit size before being shifted to higher pressures for slit sizes of about 7 Å. The reason for this is that the tetrahedral hydrogen bond network is frustrated in very small pores, thus requiring higher pressures for pore filling. While our results are in qualitative agreement, Striolo et al. observed adsorption and desorption at pressures which are smaller by about a factor of 10 shifting them below the saturation pressure. This difference cannot be explained solely by our smaller interaction as demonstrated in Figure 3. Although this sounds like an irreconcilable difference, it may be rooted in the conversion from chemical potential to relative pressure, which because of its exponential functional relationship can lead to large errors. While we have determined the chemical potential at the coexistence pressure very thoroughly as described earlier, Striolo et al. might have overestimated  $P_0$  by computing the coexistence chemical potential from GCMC simulations, which may produce metastable states near the vapor–liquid phase transition. This is also criticized in a study by Liu and Monson,<sup>41</sup> who use the Gibbs ensemble Monte Carlo to find the bulk vapor–liquid equilibrium and discover that condensation does not occur in larger slits for pressures below the bulk saturation pressure,  $P_0$ . They attribute this behavior to the lack of hydrogen bonding with the graphite surface that destabilizes dense water phases relative to the bulk water. Depending on the used water model and the exact slit width, they observe adsorption below the saturation pressure,  $P_0$ , in smaller tubes, which they ascribe to a stabilization by the strong dispersion interactions with both carbon surfaces. In agreement with our data, they find desorption at pressures below  $P_0$  for all but very small slits.

Their adsorption and desorption pressure values can be brought into approximate quantitative agreement with our results anticipating a small shift to lower pressures resulting from the difference in the interaction potential. Thus, it seems that the discrepancy between the simulated adsorption pressures and those observed in experiment is solely based on the lack of active sites in the simulations. While the change in water–carbon interaction does not seem to change the internal structure of the adsorbed water giving a similar potential energy, the slit geometry has a strong effect on the water–water potential

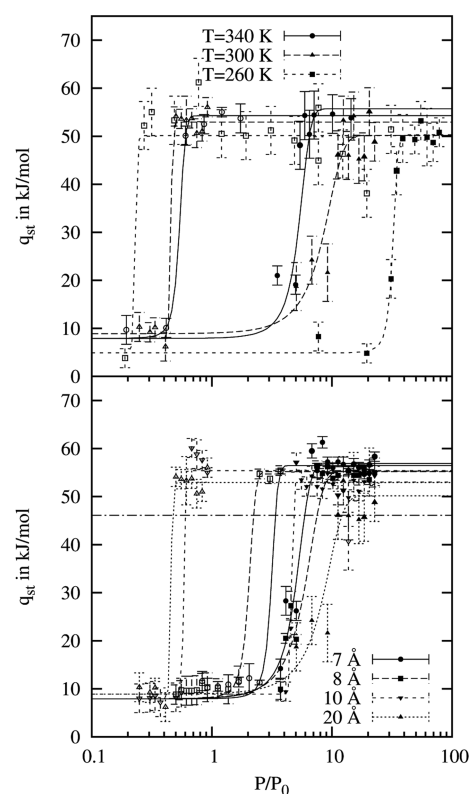


**Figure 5.** Top: Isosteric heat of adsorption at three different temperatures for a 20 Å slit. The lines are there to guide the eye. Closed symbols denote adsorption, and open symbols desorption. Bottom: Isosteric heat of adsorption for different slit geometries at 300 K. The horizontal line denotes the heat of vaporization of TIP4P/2005 water taken from Abascal and Vega.<sup>19</sup> The other lines are there to guide the eye. Closed symbols denote adsorption, and open symbols desorption.

energy per molecule, which is reduced with growing slit width. The reason for this can easily be deduced by looking at the water density distribution in Figure 4. While in a 7 Å slit only one layer of water can form allowing only for lateral water–water interaction, two and more layers exist in the larger slits. Thus, we see a rapid decrease in potential energy with growing slit width converging to its bulk value. Unfortunately, we have to conclude that because of the strong impact active sites have on the experimental adsorption curves, a comparison with simulation in order to set limits on the water–carbon interaction parameters becomes near impossible.

In addition we compute the isosteric heat of adsorption by the fluctuation formula taken from the book of Nicholson and Personage.<sup>42</sup>

$$q_{\text{st}} = - \frac{\langle UN \rangle - \langle U \rangle \langle N \rangle}{\langle N^2 \rangle - \langle N \rangle^2} + kT \quad (6)$$

Here,  $U$  is the potential energy and  $N$  is the adsorbed molecule number.

In Figure 5, bottom, we report  $q_{\text{st}}$  for different slit geometries. As the results are quite noisy, lines are added to guide the eye. The closed symbols indicate the adsorption and the open ones the desorption branch. As indicated by the horizontal line, values for  $q_{\text{st}}$  after filling of the slit exceed the value expected from the enthalpy of condensation for TIP4P/2005 water. The limit of zero coverage for  $q_{\text{st}}$  lies at around 8–9 kJ/mol, which is close

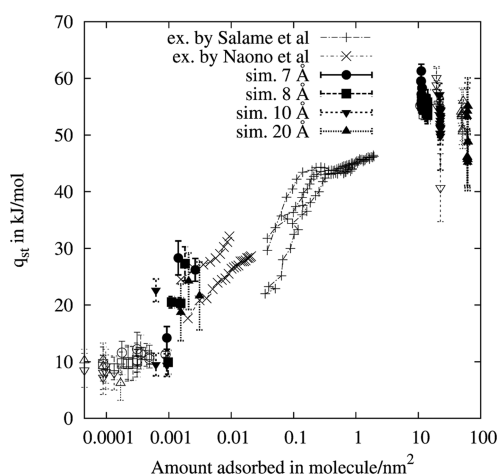
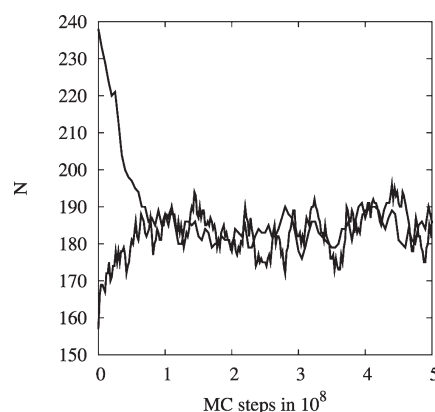


**Figure 6.** Simulated  $q_{st}$  against coverage for different slit widths at 300 K in comparison to experimental adsorption data of water on various activated carbons from Salame and Bandosz taken from Brennan et al.<sup>34</sup> and by Naono et al.<sup>43</sup> Closed symbols denote adsorption, and open symbols desorption.

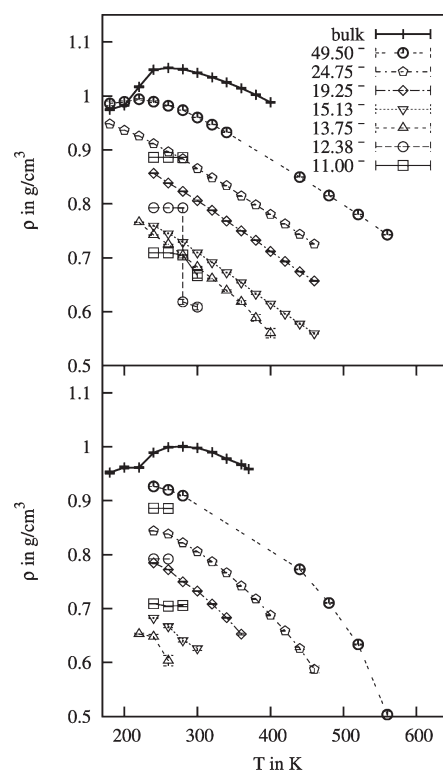
to the value found in a simulation study by Striolo et al.<sup>8</sup> using SPC/E (simple point charge/extended) water and a water–carbon interaction energy of 0.389 kJ/mol. In the pressure range close to pore filling on the adsorption branches, one can observe a rising of  $q_{st}$  to a value of  $\approx 26$  kJ/mol. This is due to the formation of small clusters of about 4–8 water molecules during the simulation. We do not include the polarization correction, which is required by all effective pair potentials that include the average effects of polarization,<sup>44</sup> in the full pressure regime. We only apply it at higher coverage, where cluster formation is visible, as isolated water molecules in the slit are only interacting by the wall–water LJ potential and are thus similar to molecules in the gas phase. Figure 5 top shows the isosteric heat of adsorption for three different temperatures. The hysteresis decreases with growing temperature, while the temperature dependence of the limiting values of  $q_{st}$  for low and high coverage is only small.

Figure 6 shows two experimental studies in comparison to our simulation results. The results of Salame and Bandosz are taken from Brennan et al.<sup>34</sup> They find a similar trend for various activated carbons. The isosteric heat rises steeply from about 20 kJ/mol reaching the heat of condensation of bulk water at a low surface coverage of about 0.6 molecules/nm<sup>2</sup>. Also shown are results from an adsorption study by Naono et al.<sup>43</sup> on AC-1 and AC-2 activated carbons. The substrates were characterized by nitrogen adsorption giving a pore size of 0.9 nm and a total surface area of 2500 and 2030 m<sup>2</sup> g<sup>−1</sup> for AC-1 and AC-2, respectively. They compute the differential adsorption enthalpies at low coverage from the Clausius–Clapeyron equation and find a steep rise from 17 to 32 kJ/mol depending on the type of carbon with growing coverage. Their values are not too far from our simulation results, where a rise from 10 to 30 kJ/mol is observed in this coverage regime.

Overall, our simulations show a similar picture to the experimental one. At very low coverage where we find only one or two molecules in a configuration,  $q_{st}$  is very low at about 8–9 kJ/mol. It grows to about 30 kJ/mol on the formation of small clusters built from about 4–8 molecules. When the clusters grow further, the pore is always filled completely, leading to a isosteric heat



**Figure 7.** Convergence of the GCMC simulation can be judged by starting from two different configurations, one above and one below the equilibrium.



**Figure 8.** Water density,  $\rho$ , vs temperature,  $T$ , for different tube diameters at 1000 atm (top) and 1 atm (bottom).

close to the condensation heat of bulk water and resulting in a jump in coverage that is determined by the slit size.

**Results for TIP4P Water in SCNTs.** In order to fill the tubes, we first perform simulations with a chemical potential high enough to allow for easy entry of water into the tube. Then we decrease the chemical potential to its correct value and equalize it before performing the actual simulation. In order to check for convergence, we try to approach the equilibrium molecule number from above as well as from below (see Figure 7). The MMM1D method<sup>45,46</sup> was used to treat long-range Coulomb interactions. And after convergence, a minimum of 500 million GCMC steps was performed to compute equilibrium values.

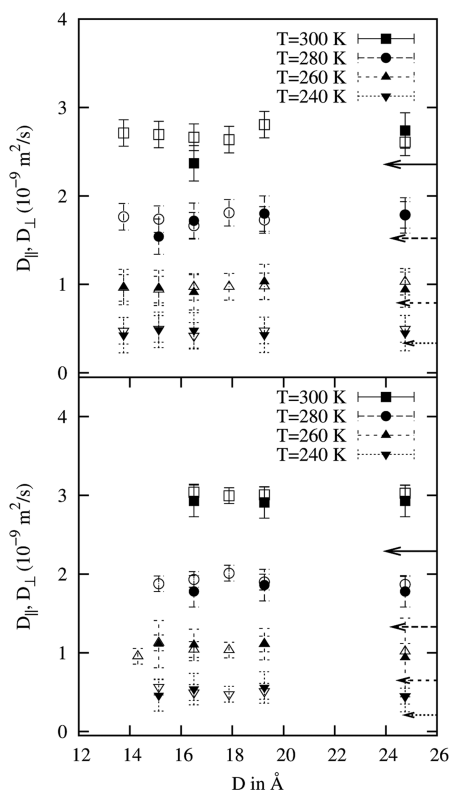


**Figure 9.** Diffusion constant along the tube axis,  $D_{\parallel}$  (open symbols), and perpendicular to the tube axis,  $D_{\perp}$  (filled symbols), vs tube diameter,  $D$ , for different temperatures at 1 atm (bottom) and at 1000 atm (top). Arrows indicate bulk diffusion constants.

**Density.** Figure 8 shows the density for different tube diameters in dependence on temperature for  $P = 1$  atm and  $P = 1000$  atm. The average particle numbers ranged from about 60 molecules for the smallest tubes to 3500 molecules for the largest. From diameters 13–25 Å, where the water in the tube is liquid, the density decreases by about 20%. This observation is in qualitative agreement with that of Alexiadis and Kassinos,<sup>18</sup> who have computed the density of water inside a carbon nanotube surrounded by a water bath at  $T = 300$  K and  $P = 1$  atm by MD simulation. We observe that the density at  $D = 25.0$  Å is still about 15% off its bulk value.

As will be demonstrated later by a structural analysis, water freezes in the two narrowest tubes, thus explaining the observed density jump. It can also be seen that for  $D = 11$  Å there exist two stable ice structures one with a higher and one with a lower density.

For narrow tubes at deep temperatures, the density curve is flat, as here the ice structure is fully occupied by water molecules. A jump in density is observed on melting, visible at  $P = 1000$  atm and  $D = 12.38$  Å between 260 and 280 K. A change in density on melting can also be observed for the low density ice form in the 11.00 Å tube at  $P = 1000$  atm between 280 and 300 K. For larger tube diameters and higher temperatures, the density seems to decrease monotonically with growing temperature. We also simulated a larger tube with diameter 49.5 Å and a length of 60 Å to demonstrate the convergence to the bulk values. Here one can also observe the development of a density maximum although less pronounced and at a temperature 40 K lower than in the bulk fluid.

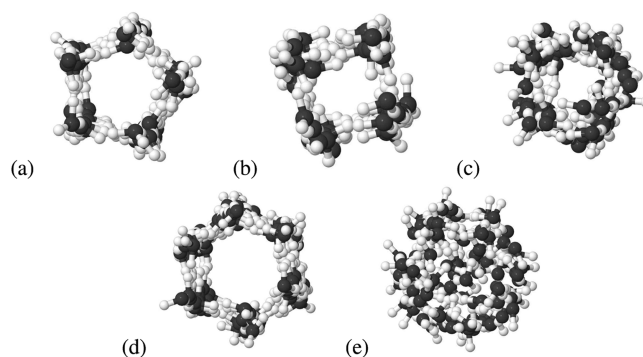


**Figure 10.** Top views of different ring and liquid structures that are stable in the  $D = 11.001$  Å (a–c) and  $D = 12.376$  Å (d,e) tubes (generated with jmol).

This indicates that the structures responsible for the development of the density maximum exist on a scale between 25 and 50 Å. They are frustrated in smaller tubes. This characteristic size corresponds to  $0.12 < q < 0.25$  1/Å in momentum space, which coincides with the enhancement that is observed in the small-angle X-ray scattering and in simulations below  $q \approx 0.4$  1/Å.<sup>47,48</sup>

**Self-Diffusion.** As stated in the book of Schoen,<sup>49</sup> it is not a trivial problem to compute the self-diffusion in confined geometries. For the time being, we will assume that the self-diffusion obeys Fick's law

$$\frac{\partial c(\vec{r}, t)}{\partial t} = \nabla \cdot \mathbf{D} \cdot \nabla c(\vec{r}, t) \quad (7)$$

where  $c(\vec{r}, t)$  is the particle density at  $\vec{r}$  and  $t$  and  $\mathbf{D}$  denotes the diffusion tensor. Although  $\mathbf{D}$  is in general time and position dependent, it can be assumed to be constant in the hydrodynamic limit approximation. As we only investigate tube geometries and all observed crystals have axis along the principal directions, we can assume that  $\mathbf{D}$  is diagonal.

$$D_{\parallel} = D_{zz} \\ D_{\perp} = \frac{1}{2}(D_{xx} + D_{yy}) \quad (8)$$

For homogeneous, isotropic bulk phases, there exists a simple formula linking the macroscopically defined diffusion tensor with microscopic quantities.

$$2D_{\alpha\alpha}t = \lim_{t \rightarrow \infty} \langle [\alpha(0) - \alpha(t)]^2 \rangle \quad (9)$$

Unfortunately, this equation does not hold for the diffusion in the confined directions, where the solution of eq 7 must match different boundary conditions. Bródka<sup>50</sup> provided an altered expression for cylindric geometries accounting for confinement. He solved the diffusion equation for a particle in an infinite cylinder of radius  $R$ , assuming reflective cylindric walls and an uniform initial particle distribution

$$\begin{aligned} & \langle [x(0) - x(t)]^2 + [y(0) - y(t)]^2 \rangle / 2 \\ &= R^2 \left[ \frac{1}{2} - 4 \sum_{n=1}^{\infty} \frac{1}{\xi_{1n}^2 (\xi_{1n}^2 - 1)} \exp \left( -\frac{\xi_{1n}^2}{R^2} D_{\perp} t \right) \right] \end{aligned} \quad (10)$$



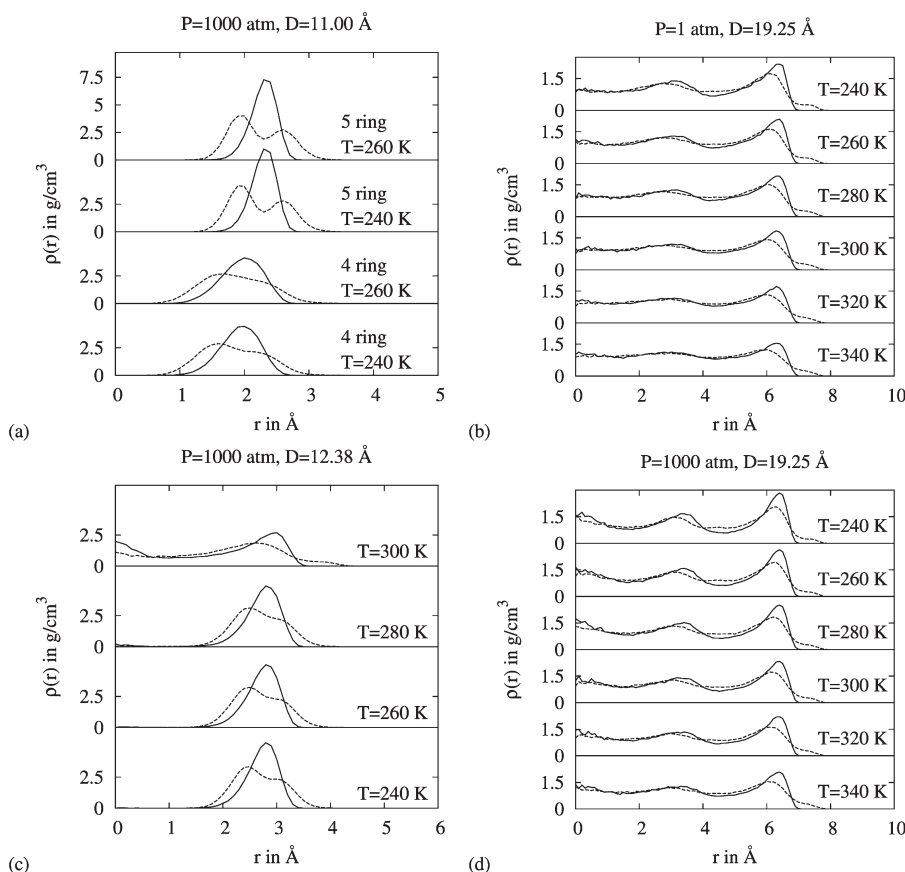


**Figure 11.** Density profiles (solid line O atoms and dashed line H atoms) in lateral direction are shown for different temperatures at  $P = 1000$  atm for tube diameters  $D = 11.00$  Å (a) and  $D = 12.38$  Å (c) as well as at  $P = 1$  atm (b) and  $P = 1000$  atm (d) for tube diameter  $D = 19.25$  Å.

Here  $\xi_{1n}$  is the  $n$ th root of the equation  $dJ_1(x)/dx = 0$  and  $J_1(x)$  is the Bessel function of order 1.

There are three caveats when using eq 10 with our data for  $\langle [\alpha(0) - \alpha(t)]^2 \rangle$ . First, they only apply to uniform particle distributions, which may only be assumed for large slits and tubes, where the layering near the surface is not important. Second, as we do not use impermeable boundaries but soft ones, there is the additional difficulty of fixing  $R$ . We decide to fit  $R$  as well as  $D_\perp$ . The results are quite reasonable as one gets values for  $R$  between the zero of the potential and the soft wall, which describe a straight line with a zero crossing of  $4.843$  Å, which is only 10% smaller than our estimate of  $2z_0$ .

Third, as noted by Striolo,<sup>51</sup> water does only diffuse according to a Fickian-type diffusion mechanism for large times. By investigating infinitely long carbon nanotubes of diameter  $10.8$  Å, Striolo finds that water molecules diffuse through a fast ballistic motion mechanism for up to 500 ps at room temperature, which changes then to Fickian. This is confirmed by Mukherjee et al.<sup>52</sup> who search for single-file diffusion in open carbon nanotubes of diameter  $8$  Å. They observe an initial phase of ballistic diffusion followed by a Fickian one in the long run. For the very small tubes investigated, they argue that the hydrogen bonds lead to a strong correlated motion similar to the ballistic mode ( $|z(t) - z(0)|^2 \propto t^2$ ), but at the same time the quasi one-dimensional structure gives rise to single-file diffusion ( $|z(t) - z(0)|^2 \propto t^{1/2}$ ), resulting in an apparent Fickian diffusivity. Thus, bulk and confined water share the same macroscopic diffusion mode.

Alexiadis and Kassinos<sup>18</sup> do not find a distinct, long period of ballistic diffusion, which they ascribe to using a higher density than Striolo, where clusters have no space to perform coordinated ballistic motion. They show that the diffusion mechanism is mainly Fickian with  $\alpha$  in  $D \propto |z(t) - z(0)|^2/t^\alpha$  varying between 1 and 0.8.

Here, we observe no long period of non-Fickian motion mechanism, but we nevertheless carried out MD runs of at least 500 ps to fit eqs 9 and 10 to the long time behavior.

A good review of past results regarding the self-diffusion of water in carbon nanotubes has been given by Alexiadis and Kassinos in 2008.<sup>53</sup> Most studies have focused on small carbon nanotubes at room temperature at 1 atm, with the most comprehensive one by Alexiadis and Kassinos themselves.<sup>18</sup> As we compute the self-diffusion for different temperatures and pressures in a wide range of tube radii, our investigation should broaden the knowledge of the dynamic behavior of water in confinement.

Regardless of all the uncertainties involved, the fit functions apply very well to our data for the larger tubes. Problems arise for the perpendicular diffusion in smaller tubes at higher temperatures, because here the diffusion is relatively large so that eq 10 reaches its plateau very quickly and a fit becomes difficult. Our final results for the perpendicular diffusion are therefore afflicted with relatively large errors and we cannot determine it for all simulated tube diameters and temperatures.

Our results for the diffusion constant are depicted in Figure 9, where the arrows indicate the bulk values. The open symbols



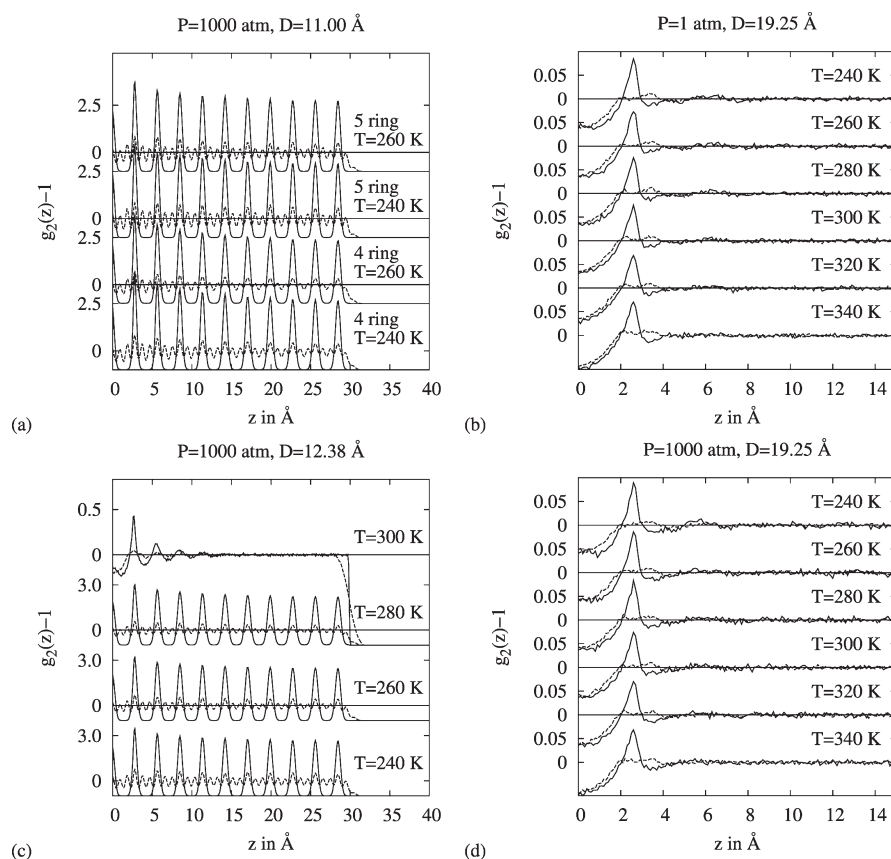


**Figure 12.** Pair correlation functions in  $z$  direction (solid line O atoms and dashed line H atoms) depicted for the same parameters as described in Figure 11. ((a)  $P = 1000$  atm,  $D = 11.00$  Å; (b)  $P = 1$  atm,  $D = 19.25$  Å; (c)  $P = 1000$  atm,  $D = 12.38$  Å; and (d)  $P = 1000$  atm,  $D = 19.25$  Å).

denote the parallel diffusion, and the filled symbols the perpendicular one. As for the density, the diffusion values are still somewhat away from the bulk values even for our widest tubes. Generally, the diffusion in the tubes lies somewhat above the unconfined one.

This behavior might seem extraordinary as one would expect a decrease in the self-diffusion constant in confinement as the movement of the molecules is restricted. But it has already been shown experimentally that a fast molecular transport takes place in carbon nanotubes, e.g., by Holt et al.<sup>17</sup> Our results are thus in general agreement with that of Alexiadis and Kassinos<sup>18</sup> at  $T = 300$  K, although the enhancement in the self-diffusion is less pronounced in their study. They observe that the deviation from the bulk behavior is minimal for tube diameters larger than 20 Å and the diffusion constant is only slowly drifting away from its bulk value, increasing with decreasing diameter. Figure 9 also demonstrates that the diffusion perpendicular to the tube axis is of the same size as the axial one and does not seem to change too much with the tube diameter, although we can only draw conclusions about relatively moderate tube radii.

**Structure and Potential Energy.** A number of papers discussing the structural behavior of water enclosed in carbon nanotubes of different radii were published in the past few years. It is difficult to analyze the data for a precise comparison, as the used water models, carbon potentials, and simulation setups differ widely between different studies.

In our simulations, we observe stacked ring structures in (8,8) and (9,9) SWNTs (see Figure 10a, b, and d) and a order-to-disorder transition in the (8,8) SWNT (see Figure 10b to c) and in the (9,9) SWNT (see Figure 10d to e). While the melting

transition from the hexagonal phase (d) to the liquid (e) is accompanied by a jump in density and potential energy, we observe only a moderate change for the transition from the square phase (b) to the liquid (c). Generally, we observe that the high density pentagonal phase (a) seems to transform to square ice (b) before melting (c). This is in agreement with Koga et al.,<sup>4</sup> who additionally found heptagonal ice structures, and Byl et al.,<sup>5</sup> who observe also 8-ring and 9-ring ice structures that do not occur in our simulations. Koga et al. argue that the difference in the solid–liquid transition of 4-ring ice and larger ring ice structures is connected to the symmetry change that occurs in the bigger tubes between the ice ring structure and the liquid structure, where molecules are also located in the center of the tube. In the small tubes, there is not enough space even in the liquid state for molecules to be located outside the first layer of molecules adsorbed on the surface. Thus, the ring structure is preserved.

The structural order can also be seen in Figures 11 and 12. For the  $D = 11$  Å tube, it is easy to differentiate between the two different ice forms in the radial density profile at  $P = 1000$  atm (see Figure 11a). The pair correlation function in the  $z$ -direction shows the strong correlation signaling the ordered ice state (see Figure 12a). The structure with the higher potential energy consists of stacked rings that are formed of 4 water molecules each (see Figure 10b) and seems less ordered than the second structure that is formed out of stacked 5 molecule rings (see Figure 10a).

For higher temperatures, the 4-ring ice structure gets more and more disordered. Although there are still 4 molecules in each layer, they are no longer stacked exactly above each other

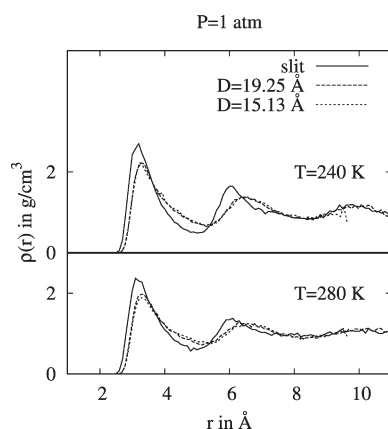


**Figure 13.** Radial density profile is shown for a slit geometry with width 50 Å and two tubes of diameters 19.25 and 15.13 Å at identical thermodynamic conditions.

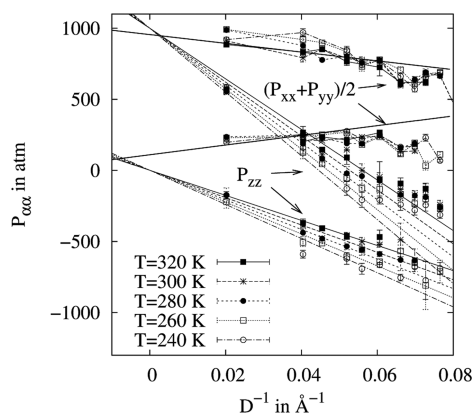


**Figure 14.** Diagonal components of the pressure tensor vs the inverse tube diameter for different temperatures and two pressures, 1 atm (lower data sets) and 1000 atm (upper data sets).

(see Figure 10c). As the radial density profile is not fundamentally changed by the melting transition in the 11.00 Å tube, we only observe a slow broadening with temperature. Next we investigate tubes of diameter  $D = 12.376$  Å. Here we observe a transition from a frozen ordered 6-stacked-ring structure with low diffusion constant, low potential energy, and higher density at low temperatures and high pressures (see Figure 10d) to a liquid network structure with high diffusion constant, higher potential energy and lower density at higher temperatures and lower pressures (see Figure 10e). The order-to-disorder transition can also clearly be seen in the density profile as well as in the  $z$ -pair correlation function (see Figures 11c and 12c).

As mentioned before, similar freezing transitions from 7 and 8 stacked rings to network structures were observed by Byl et al. and Striolo et al. for tubes of diameter  $D = 13.751$  Å.<sup>4,5,9</sup> We do not observe stacked-ring structures in the investigated temperature and pressure range for this tube size. But our radial oxygen and hydrogen density profiles for the (8,8) and (10,10) nanotubes are in good agreement with those presented by Striolo et al.<sup>9</sup> For wider tubes, the structural changes with temperature and pressure are only weak, showing a general strengthening of the pair correlation with increasing pressure and decreasing temperature (see Figures 11b,d and 12b,d). This is in agreement

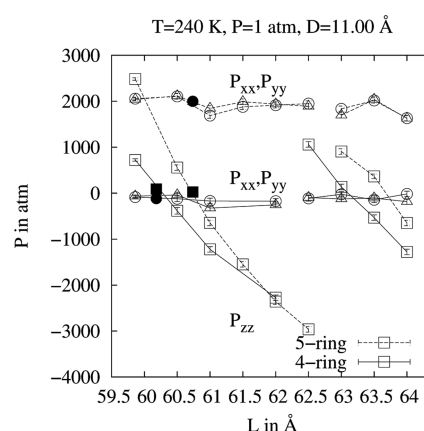


**Figure 15.** Dependence of the pressure components on the tube length,  $L$ , for the 4-ring and 5-ring ice tubes (open symbols). Also shown are the equilibrium lengths from the constant pressure simulations (filled symbols). Solid lines indicate 5-ring, and dashed ones 4-ring structures (triangles,  $P_{xx}$ ; circles,  $P_{yy}$ ; squares,  $P_{zz}$ ).

with earlier studies as no transitions have been observed for larger tubes in the literature.

More insight into the structural effect of confinement can be gained by comparison between the radial density profiles in a slit geometry with the same interaction parameters and at the same thermodynamical conditions (see Figure 13). The slit has a large diameter of 50 Å in order to get density profiles similar to the ones near a single wall.

It is easy to see that the limited space inside the tubes puts strain on the water structure that gives rise to significant difference in peak height and position in the density profile.

**Pressure.** The diagonal components of the pressure tensor vs the inverse tube diameter are shown in Figure 14. With increasing tube diameter, the pressure approaches the bulk pressure, although the convergence is slow. But as we have already established by looking at the density and the diffusion, we are still far away from bulk behavior even for our widest tubes. (For example, if the surface induced structure extends over 10 Å, then only 40% of the widest tube's volume is bulk water.) Extrapolation of the  $P_{zz}$  data in Figure 14 yields bulk pressures for tube diameters above 500 Å. The pressure measured in the direction of the tube axis shows an approximate linear dependence in  $D^{-1}$ . This is in agreement with Laplace's law for the capillary pressure<sup>54</sup>

$$P = P_{\text{bulk}} - \frac{2\gamma \cos(\theta)}{R} \quad (11)$$

where  $\gamma$  is the surface tension and  $\theta$  is the contact angle of water on graphite. We take experimental values of the surface tension at 1 atm from Vargaftik et al.<sup>55</sup> and extrapolate to lower temperatures. As we could not find values for  $\gamma$  at 1000 atm, we extrapolate them linearly assuming a value of 6.96 Å for  $(d\gamma/dP)_{T_{\text{An}}}$  taken from Kathmann et al.<sup>56</sup> The contact angle of water on graphite was measured by Osborne,<sup>57</sup> showing an approximate linear change with temperature with a slope of 0.04 K<sup>-1</sup>. Thus we assume  $\theta(T) = \theta_{300\text{K}} + 0.04 \text{ K}^{-1} \times (T - 300 \text{ K})$ , leaving only  $\theta_{300\text{K}}$  as a fit parameter. We arrive at a contact angle of  $\approx 70^\circ$ , which is about 14° smaller than the angle found by Osborne.<sup>57</sup> It is interesting that this continuum limit approach is in very reasonable accord with the simulations as shown in Figure 14. Obvious deviations only occur below  $D \approx 20$  Å especially at low pressure.

While the pressure in the liquid phase is independent of the tube length,  $L$ , this is not the case for the ice ring structures. Figure 15 shows the change in pressure with changing tube length for the 4-ring and 5-ring ice structures at  $T = 240$  K and  $P = 1$  atm. While the lateral pressure components are basically constant with  $L$ ,  $P_{zz}$  changes strongly. One can observe a periodic behavior as  $L$  is increased sufficiently to allow another molecular layer to form. As the ice structure turns unstable for very large negative pressures, we also performed  $\mu$ PT ensemble Monte Carlo computations to fix the pressure in  $z$  direction to 1 or 1000 atm. The resulting equilibrium lengths are also included in Figure 15.

## CONCLUSION

Concerning the used carbon–water interaction potential, we found that the condensation transition occurs above the saturation pressure for all slit widths considered, while evaporation happens below  $P_0$  for larger slits. For a stronger carbon–water interaction, evaporation and condensation are shifted to smaller pressures. In order to estimate the true interaction strength between carbon and water, experiments on substrates without active sites on the surface and a well-defined pore size distribution would be mandatory. Nevertheless, the simulated isosteric heats of adsorption as a function of the coverage are in good accord with the experiments.

Regarding our tube simulations, we learned that the suppression of the density maximum in tubes with  $D$  below 50–25 Å indicates that “cluster” structures thought to be responsible for this anomaly are of comparable size. In scattering experiments, these structures correspond to  $0.25 \text{ Å}^{-1} > q > 0.12 \text{ Å}^{-1}$ , where  $q$  is the magnitude of the scattering wave vector. In smaller tubes, these constrictions lead to a varied phase behavior with the occurrence of several different ice nanotubes. The axial pressure is well described within the continuum limit. Deviations become apparent for  $D < 20$  Å, while extrapolation shows that CNTs containing bulk water must at least be 500 Å in diameter. The diffusion characteristics of confined water are similar to that of bulk water, demonstrating that while the structure of the hydrogen bond network is constricted its agility seems to be preserved. The fast water transport through carbon nanotubes that is found experimentally confirms this conclusion. Therefore, the determination of water’s properties below the homogeneous nucleation line in larger sized nanopores seems feasible.

## AUTHOR INFORMATION

### Corresponding Author

\*E-mail: hentschk@uni-wuppertal.de.

## REFERENCES

- (1) Mallamace, F.; Broccio, M.; Corsaro, C.; Faraone, A.; Wanderlingh, U.; Liu, L.; Mou, C. Y.; Chen, S. H. *J. Chem. Phys.* **2006**, *124*, 161102–161106.
- (2) Chen, S.-H.; Mallamace, F.; Mou, C.-Y.; Broccio, M.; Corsaro, C.; Faraone, A.; Liu, L. *Proc. Natl. Acad. Sci. U.S.A.* **2006**, *103*, 12974–12978.
- (3) Kumar, P.; Buldyrev, S. V.; Stanley, H. E. *NATO Sci. Ser., II* **2007**, *23*–36.
- (4) Koga, K.; Gao, G. T.; Tanaka, H.; Zeng, X. C. *Nature* **2001**, *412*, 802–805.
- (5) Byl, O.; Liu, J.-C.; Wang, Y.; Yim, W.-L.; Johnson, J. K.; Yates, J. T. *J. Am. Chem. Soc.* **2006**, *128*, 12090–12097.
- (6) Martí, J.; Gordillo, M. C. *Phys. Rev. B* **2001**, *63*, 165430–165435.
- (7) Martí, J.; Gordillo, M. C. *Phys. Rev. E* **2001**, *64*, 021504–021510.
- (8) Striolo, A.; Chialvo, A. A.; Cummings, P. T.; Gubbins, K. E. *Langmuir* **2003**, *19*, 8583–8591.
- (9) Striolo, A.; Chialvo, A. A.; Gubbins, K. E.; Cummings, P. T. *J. Chem. Phys.* **2005**, *122*, 234712–234714.
- (10) Striolo, A.; Chialvo, A. A.; Cummings, P. T.; Gubbins, K. E. *J. Chem. Phys.* **2006**, *124*, 074710–074721.
- (11) Birkett, G. R.; Do, D. D. *J. Phys. Chem. C* **2007**, *111*, 5735–5742.
- (12) Hummer, G.; Rasaiah, J. C.; Noworyta, J. P. *Nature* **2001**, *414*, 188–190.
- (13) Sansom, M. S.; Biggin, P. C. *Nature* **2001**, *414*, 156–159.
- (14) Kalra, A.; Garde, S.; Hummer, G. *Proc. Natl. Acad. Sci. U.S.A.* **2003**, *100*, 10175–10181.
- (15) Pascal, T. A.; Goddard, W. A.; Jung, Y. *Proc. Natl. Acad. Sci. U.S.A.* **2011**, *108*, 11794–11798.
- (16) Guse, C.; Simionescu, A.; Schünemann, B.; Hentschke, R.; Bomsdorf, H. J. *Phys.: Condens. Matter* **2010**, *22*, 325105–325114.
- (17) Holt, J. K.; Park, H. G.; Wang, Y.; Stadermann, M.; Artyukhin, A. B.; Grigoropoulos, C. P.; Noy, A.; Bakajin, O. *Science* **2006**, *312*, 1034–1037.
- (18) Alexiadis, A.; Kassinos, S. *Mol. Simul.* **2008**, *34*, 671–684.
- (19) Abascal, J. L. F.; Vega, C. *J. Chem. Phys.* **2005**, *123*, 4505–4517.
- (20) Widom, B. *J. Chem. Phys.* **1963**, *39*, 2808–2812.
- (21) Jackson, J. L.; Klein, L. S. *Phys. Fluids* **1964**, *7*, 228–232.
- (22) Shing, K. S.; Gubbins, K. E. *Mol. Phys.* **1982**, *46*, 1109–1128.
- (23) Pi, H. L.; Aragonés, J. L.; Vega, C.; Noya, E. G.; Abascal, J. L. F.; Gonzalez, M. A.; McBride, C. *Mol. Phys.* **2009**, *107*, 365–374.
- (24) Vega, C.; Abascal, J. L. F.; Nezbeda, I. *J. Chem. Phys.* **2006**, *125*, 034503–034509.
- (25) Wang, N.; Tang, Z. K.; Li, G. D.; Chen, J. S. *Nature* **2000**, *408*, 50–51.
- (26) Stan, G.; Cole, M. W. *Surf. Sci.* **1998**, *395*, 280–291.
- (27) Wang, J.; Zhu, Y.; Zhou, J.; Lu, X. *Phys. Chem. Chem. Phys.* **2004**, *6*, 829–835.
- (28) Rana, M.; Chandra, A. *J. Chem. Sci.* **2007**, *119*, 367–376.
- (29) Werder, T.; Walther, J. H.; Jaffe, R. L.; Halicioglu, T.; Koumoutsakos, P. *J. Phys. Chem. B* **2003**, *107*, 1345–1352.
- (30) Bojan, M. J.; Steele, W. A. *Langmuir* **1987**, *3*, 1123–1127.
- (31) Talu, O.; Meunier, F. *AIChE J.* **1996**, *42*, 809–819.
- (32) Pierce, C.; Smith, R. N.; Wiley, J. W.; Cordes, H. *J. Am. Chem. Soc.* **1951**, *73*, 4551–4557.
- (33) Müller, E. A.; Rull, L. F.; Vega, L. F.; Gubbins, K. E. *J. Phys. Chem.* **1996**, *100*, 1189–1196.
- (34) Brennan, J. K.; Bandosz, T. J.; Thomson, K. T.; E, K. E. *G. K. Colloids Surf., A* **2001**, *187*–188, 539–568.
- (35) Arnold, A.; Joannis, J. D.; Holm, C. *J. Phys. Chem.* **2002**, *117*, 2496–2502.
- (36) Leung, K.; Luzar, A.; Bratko, D. *Phys. Rev. Lett.* **2003**, *90*, 65502–65506.
- (37) Kaneko, K.; Cracknell, R. F.; Nicholson, D. *Langmuir* **1994**, *10*, 4606–4609.
- (38) Ohba, T.; Kaneko, K. *J. Phys. Chem. B* **2002**, *106*, 7171–7176.
- (39) Gregg, S. J.; Sing, K. S. W. *Adsorption, surface area, and porosity*; Academic Press: London, 1991.
- (40) Kaneko, K.; Hanzawa, Y.; Iiyama, T.; Kanda, T.; Suzuki, T. *Adsorption* **1999**, *5*, 7–13.
- (41) Liu, J. C.; Monson, P. A. *Langmuir* **2005**, *21*, 10219–10225.
- (42) Nicholson, D.; Parsonage, N. G. *Computer simulation and the statistical mechanics of adsorption*; Academic Press: London, NY, 1982.
- (43) Naono, H.; Hakuman, M.; Shimoda, M.; Nakai, K.; Kondo, S. *J. Colloid Interface Sci.* **1996**, *182*, 230–238.
- (44) Berendsen, H. J. C.; Grigera, J. R.; Straatsma, T. P. *J. Phys. Chem.* **1987**, *91*, 6269–6271.
- (45) Arnold, A.; Holm, C. *J. Chem. Phys.* **2005**, *123*, 144103–144108.
- (46) Bródka, A. *J. Chem. Phys.* **2006**, *125*, 107103–107112.

- (47) Huang, C.; Wikfeldt, K. T.; Tokushima, T.; Nordlund, D.; Harada, Y.; Bergmann, U.; Niebuhr, M.; Weiss, T. M.; Horikawa, Y.; Leetmaa, M. *Proc. Natl. Acad. Sci. U.S.A.* **2009**, *106*, 15214–15219.
- (48) Sedlmeier, F.; Horinek, D.; Netz, R. R. *J. Am. Chem. Soc.* **2011**, *133*, 1391–1398.
- (49) Schoen, M. *Computer simulation of condensed phases in complex geometries*; Springer-Verlag: Berlin, Heidelberg: 1993.
- (50) Bródka, A. *Mol. Phys.* **1994**, *82*, 1075–1078.
- (51) Striolo, A. *Nano Lett.* **2006**, *6*, 633–639.
- (52) Mukherjee, B.; Maiti, P. K.; Dasgupta, C.; Sood, A. K. *J. Chem. Phys.* **2007**, *126*, 124704–1247012.
- (53) Alexiadis, A.; Kassinos, S. *Chem. Rev.* **2008**, *108*, 5014–5034.
- (54) de Gennes, P.; Brochard-Wyart, F.; Quere, D. *Capillarity and Wetting Phenomena: Drops, Bubbles, Pearls, Waves*, 1st ed.; Springer: New York: 2003.
- (55) Vargaftik, N. B.; Volkov, B. N.; Voljak, L. D. *J. Phys. Chem. Ref. Data* **1983**, *12*, 817–820.
- (56) Kathmann, S. M.; I-Feng, W. K.; Mundy, C. J. *J. Am. Chem. Soc.* **2008**, *130*, 16556–16561.
- (57) Osborne, K. L. *J. Colloid Interface Sci.* **2009**, *116*, 1–80.